Unraveling the Origin of Chirality from Plasmonic Nanoparticle-Protein Complexes

Qingfeng Zhang[1,2], Taylor Hernandez[1], Kyle W. Smith[1,#], Seyyed Ali Hosseini Jebeli[3], Alan X. Dai[4], Lauren Warning[1], Rashad Baiyasi[3], Lauren A. McCarthy[1], Hua Guo[5], Dong-Hua Chen[6], Jennifer A. Dionne[7], Christy F. Landes[1,2,3]*, Stephan Link[1,2,3]*

[1] Department of Chemistry, Rice University, 6100 Main Street, Houston, Texas 77005, USA

[2] Smalley-Curl Institute, Rice University, 6100 Main Street, Houston, Texas 77005, USA

[3] Department of Electrical and Computer Engineering, Rice University, 6100 Main Street, Houston, Texas 77005, USA

[4] Department of Chemical Engineering, Stanford University, Stanford, CA 94305, USA

[5] Department of Materials Science and Nanoengineering, Rice University, 6100 Main Street, Houston, Texas 77005, USA

[6] Department of Structural Biology, Stanford University, Stanford, CA 94305, USA

[7] Department of Materials Science and Engineering, Stanford University, Stanford, CA 94305, USA

Current Affiliation: Draper Laboratory 555, Technology Square Cambridge, MA 02139, USA

*Corresponding Author. Email: clandes@rice.edu (C.F.L.); slink@rice.edu (S.L.)

One Sentence Summary: Plasmon-coupled circular dichroism from nanoparticle-protein complexes is dominated by nanoparticle aggregation, forming both chiral aggregates and electromagnetic hotspots for amplifying and transducing protein chirality.

Abstract

Plasmon-coupled circular dichroism has emerged as an intriguing approach for ultrasensitive detection of biomolecular conformations through coupling between molecular chirality and surface plasmons. Chiral nanoparticle assemblies without chiral molecules present also have large optical activities. We apply single-particle circular differential scattering spectroscopy coupled with electron imaging and simulations to identify both structural chirality of plasmonic aggregates and plasmon-coupled circular dichroism induced by chiral proteins. We establish that both chiral aggregates and just a few proteins in interparticle gaps of achiral assemblies are responsible for the ensemble signal, but single nanoparticles do not contribute. We furthermore find that the protein plays two roles: it transfers chirality to both chiral and achiral plasmonic substrates and it is also responsible for the chiral 3D assembly of nanorods. Understanding these underlying factors paves the way toward sensing the chirality of single biomolecules.

Sensitive detection of the chirality of a biomolecule is of great interest to the field of drug development because it plays a key role in molecular recognition and function (*1-4*). By exploiting the strong electromagnetic near-fields in plasmonic nanostructures (*5-9*), theoretical (*10-12*) and experimental (*10, 13-15*) studies reveal enhanced circular dichroism (CD) intensities for biomolecular adsorbates, and, intriguingly, a new chiral plasmon resonance. This plasmon-coupled circular dichroism (PCCD) is thought to originate from dipole-dipole interactions between the chiral adsorbate and the plasmonic nanoparticle (NP) (*10, 14*), creating a large CD signal in the more easily accessible visible spectral range. However, PCCD has so far exclusively been measured with ensemble techniques, with contradicting conclusions (*10, 13-21*).

A major difficulty for sensing chiral biomolecules with ensemble PCCD spectroscopy in solution is the potential presence of even a few NP aggregates with chiral configurations that can yield stronger CD signals than PCCD (*13, 17, 22*). Structural chirality of NP assemblies has been well established on both ensemble and single-NP levels,(*8, 9, 23, 24*) but is generally ignored for PCCD because ensemble analyses cannot distinguish small subpopulations. The need for high ionic strength buffers when working with biomolecules makes some NP aggregation an important consideration. Another question is whether all biomolecules contribute equally to the PCCD signal or if biasing occurs for molecules located in interparticle gaps where the electromagnetic fields are the highest.

To address these outstanding issues, we take advantage of the varying gold nanorod (Au NR)-bovine serum albumin (BSA) complexes that form depending on the relative abundance of NRs and protein. At high BSA concentrations, a protein monolayer on each NR ensures a stable colloidal solution, whereas at low BSA concentrations, the NRs aggregate, triggered by partial

unfolding of individual proteins on NRs (supplementary materials, Fig. S1-S3) (*25*). This relation provides a model system with access to a range of protein-NR configurations including individual NRs covered with a protein monolayer, aggregates with few proteins that are also structurally chiral, and all intermediate combinations. To distinguish these subpopulations in a complex mixture, we used single-particle circular differential scattering (CDS) spectroscopy (*26*). For the 343 nanostructures analyzed, only aggregated NR-BSA complexes were CDS active but no single NRs were CDS active, in direct contrast to many ensemble PCCD studies (*10, 14-19, 21*). We also present evidence for both structural chirality and PCCD for BSA located in electromagnetic "hotspots."

Although strong ensemble PCCD was observed at the plasmon resonance for low BSA concentrations, single-particle CDS spectroscopy with correlated electron microscopy on the individual components of the ensemble revealed that no single NR-BSA complexes have detectable CDS (Fig. 1, A and B, and Fig. S4, S5). The same is true for single NRs with a BSA monolayer (Fig. S6). Considering that a perfect single Au NR is achiral (Fig. S7), the absence of CDS is likely the result of low electric-field enhancement of a single Au NR and weak coupling based on poor spectral overlap between the CD signal of BSA in the ultraviolet and the plasmon resonance in the visible (*27*).

In contrast to single Au NRs, the majority of NR-BSA aggregates exhibit CDS (Fig. 1C and Fig. S8-S10). Based on the statistical distribution of different subpopulations (single NRs and aggregates of different sizes) and their respective CDS activity (Fig. 1D), we conclude that a subpopulation of aggregates was responsible for the observed ensemble PCCD signal (Fig. 1A). This conclusion is not affected by the type of supporting substrate (Fig. S11). We propose two potential origins for the CDS of aggregates: (i) Intrinsic structural chirality is present in the

aggregates and is dominated by right-handed configurations to create an enantiomeric excess and the PCCD line shape in Fig. 1A (*21*); and (ii) closely spaced NRs create electromagnetic hotspots that substantially enhance BSA-induced PCCD, supported further by the same handedness of PCCD in the visible and CD of BSA in the ultraviolet (Fig. S12) (*14, 25, 28*).

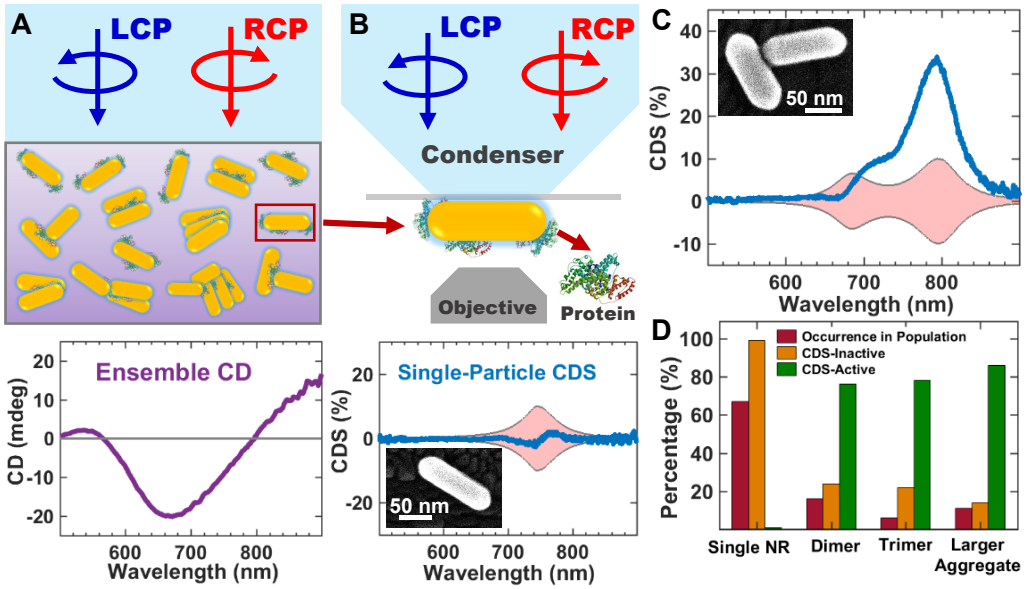

Fig. 1. Single-particle CDS spectroscopy establishes the role of nanoparticle aggregation in ensemble PCCD of Au NR-BSA complexes. (**A**) Schematic illustration of ensemble CD measurements (top) and PCCD spectrum (bottom) of Au NR-BSA complexes at [BSA] = 1.5 μM (LCP/RCP: left/right-handed circularly polarized light). (**B**) Schematic illustration of single-particle CDS measurements (top) and CDS spectrum (bottom) for a single Au NR-BSA complex. The inset shows the correlated SEM image. (**C**) CDS spectrum of single Au NR dimer-BSA complex. The inset shows the correlated SEM image. The experimental spectra are shown with a pink envelope that represents the experimental error. (**D**) Distribution of different subpopulations sorted by aggregate size after the sample of Au NR-BSA complexes was spin-coated onto indium tin oxide (ITO) glass substrates and the corresponding percentages of CDS-active and CDS-inactive nanostructures. This data clearly shows that only aggregates produce a measurable CDS signal.

To distinguish between structural chirality and PCCD, we use high-angle annular dark field scanning transmission electron microscopy (HAADF-STEM) imaging at different tilt angles, tomographic reconstruction, and finite difference time domain (FDTD) simulations (Fig. 2). We focus primarily on smaller aggregates, dimers, and trimers, and distinguish them based on parallel versus nonparallel alignment (Fig. S13). Tomographic reconstruction was necessary to precisely visualize three-dimensional geometries including NR sizes as well as interparticle gaps, offsets,

twists, and planar displacements, which are all key factors influencing structural chirality (*26, 29*). Figure 2A shows a series of HAADF-STEM images for a nonparallel dimer together with the geometric models obtained from tomographic reconstruction (Fig. S14, Movie S1) that served as input for the FDTD simulations. The dimer was CDS active with a strong signal at 720 nm (Fig. 2B). The simulated scattering and CDS spectra were in good agreement with the experimental results (Fig. 2C and Fig. S15), confirming that this dimer was chiral. It is important to note that based on our single-particle measurements we cannot rule out effects arising from planar 2D chirality, although our previous CDS measurements could only be interpreted by assuming that the 3D chiral conformations of assembled aggregates were at least partially retained on a substrate (*26, 29*). Intriguingly, differences between the experiment and theory at 805 nm could be explained by PCCD of BSA in the interparticle gap, which the simulations could not describe. The calculated charge plots at 720 nm and 805 nm let us assign both modes to bright bonding plasmons based on plasmon hybridization theory (Fig. 2C and Fig. S16) (*5*). The resulting near-field enhancement factors ($|E/E_0|^2$) demonstrated the existence of plasmonic hotspots at the interparticle gap (*7*) that are ideal for enhancing the PCCD of BSA. As further discussed below, BSA was present in the gaps, because without BSA, there was no aggregation (*25*). Partially unfolded BSA is expected to still yield a chiral signal (*30*).

We next examined a parallel dimer-BSA complex in which CDS is observed, despite tomographic reconstruction and simulations confirming that the structure is achiral (Fig. 2, E to G, Fig. S15, Movie S2) even when considering the recently suggested possibility that the NR plasmon modes could have intrinsic offsets from the long NR axes (Fig. S17). (*31*). Analysis of the simulated scattering spectrum through charge plots and plasmon hybridization theory revealed two plasmon modes, a bonding mode at 618 nm from the coupling between two transverse oscillations

and an anti-bonding mode at 670 nm caused by interactions between the individual longitudinal resonances (Fig. 2G and Fig. S18). Interestingly, CDS was found experimentally only for the 618 nm resonance. The requirement of hotspots for PCCD explains this observation. For an achiral dimer, the calculated near-field enhancement $|E/E_0|^2$ was ~33 times larger in the interparticle gap at 618 nm compared to 670 nm (Fig. 2H), which is readily understood based on the stronger coupling of the transverse modes in this direction. Again, because aggregation is triggered by proteins (*25*), BSA is expected in the gap between the NRs, which was also independently confirmed by Raman spectroscopy (Fig. S19). Based on the volume of the gap and the size of BSA in its native state we estimate that a maximum of five folded proteins could fit (Fig. S14). We actually expect the number of molecules in the gap to be on the order of just one or a few proteins, as we have previously shown that only a single BSA binds to a NR at low relative BSA concentrations (*25*), suggesting that single-molecule PCCD should be achievable. Indeed, when lowering the BSA concentration by a factor of 100 to achieve a 1:1 NR:BSA mixing ratio, we observed the same ensemble and single-particle results as discussed in Fig. 1 and 2 (Fig. S20).

Our results of enhancing spectroscopic signals of analytes located in plasmonic hotspots are consistent with surface-enhanced Raman scattering (SERS) (*32*) but are demonstrated here for PCCD. Similarly, single-particle experiments revealed that the ensemble SERS signal arose from Raman active molecules located in the hotspots of subpopulations of aggregates, making the ultimate detection limit of a single analyte achievable (*33, 34*). The large electric fields of the hotspots are required to amplify a weak Raman scattering cross section. For PCCD, we instead needed to overcome poor spectral overlap. To illustrate that the achiral dimer in Fig. 2 is not the exception, we present another example in Fig. S21. In addition, we confirmed that the PCCD for these parallel dimers required BSA by forming achiral NR dimers via NaCl-induced aggregation,

which did not exhibit PCCD (Fig. S22). This comparison to random, salt mediated aggregation furthermore suggests another role of BSA, as discussed below.

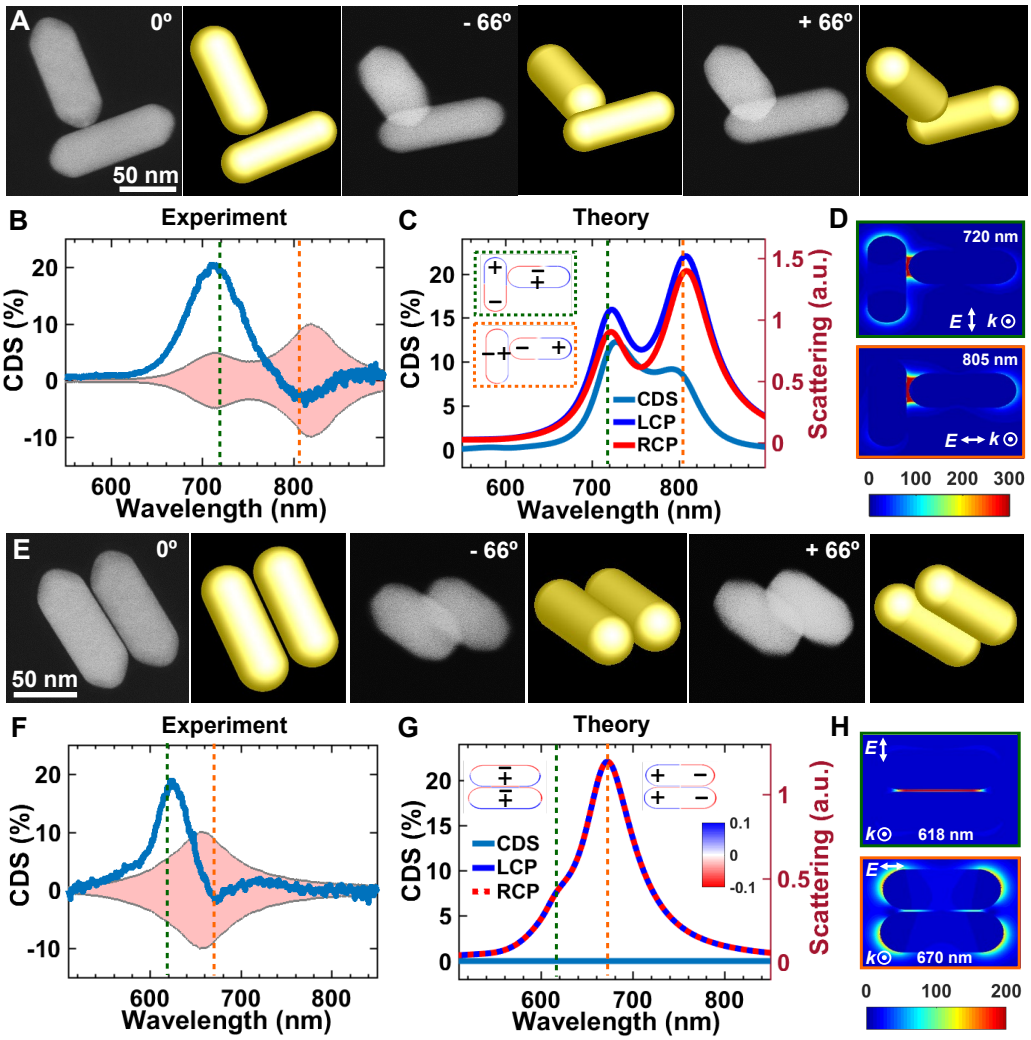

Fig. 2. CDS-active Au-NR dimer-BSA complexes with chiral (A-D) and achiral (E-H) configurations. (**A,E**) HAADF-STEM tilt series images of a chiral dimer (A) and an achiral dimer (E) and the corresponding geometric models extracted from the tomographic reconstructions. (**B,F**) Experimental single-particle CDS spectra of the chiral dimer (B) from panel A and the achiral dimer (F) from panel E. The experimental spectra are shown with a pink envelope that represents the experimental error. (**C,G**) Simulated scattering spectra of the chiral dimer (C) and achiral dimer (G) for incident LCP and RCP light and the corresponding CDS spectra. The insets in panel C show the charge plots calculated at 720 nm and 805 nm. The insets in panel G show the charge plots calculated at 618 nm and 670 nm. The charge plots in panel C and G share the same scale bar. The dashed lines in panel C and D refer to the plasmon modes at 720 nm (green) and 805 nm (orange). The dashed lines in panel F and G refer to the plasmon modes at 618 nm (green) and 670 nm (orange). (**D,H**) Cross-sectional views of calculated near-field enhancements ($|E/E_0|^2$) for the chiral dimer (D) at 720 nm and 805 nm, and the achiral dimer (H) at 618 nm and 670 nm. These results demonstrate that although the dimer in (E-H) is not chiral based on its geometry CDS is observed and must originate from chiral BSA molecules located in inter-NR "hotspots".

Analyzing the distributions of CDS activity and creating subensemble averaged CDS spectra for the various subpopulations allowed us to directly relate single-particle spectroscopy of a dried sample with the solution behavior measured by ensemble techniques. Fig. 3A compares histograms of CDS signal for NaCl-induced and BSA-induced NR aggregates. Single NRs with protein monolayers are also included as a control and showed no CDS activity. The absence of ensemble PCCD in NaCl-induced NR aggregates was explained by CDS because a racemic mixture of chiral aggregates is created (Fig. S23). Example CDS spectra of two chiral NaCl-assembled dimers with opposite handedness are shown in Fig. S24. In contrast, BSA-induced NR-BSA complexes were mostly right-handed. These conclusions were further supported by the sub-ensemble averaged CDS spectra considering either only the aggregates (Fig. 3B) or all particles present in solution (Fig. S25). In particular, for the NR aggregate-protein complexes, the dominance of one handedness and its sign matched the ensemble solution CD spectrum (Fig. 1A), as well as the ensemble CD spectrum taken for a sample deposited and dried on a glass substrate (Fig. S26). Although this comparison confirmed our single-particle approach to explain an ensemble level effect, we were unable to exclude the possibility that the contributions from structural chirality and PCCD are different in solution and on a substrate. The single-particle measurements seem to indicate that structural chirality is the dominating factor, but the presence of a substrate could bias this conclusion and the relative contributions could differ in solution. We indeed have some evidence of excitation geometry-dependent chirality (Fig. S27).

Because the preferred handedness with BSA could be caused by either PCCD or structural chirality,(*20, 21, 23*) the geometries of BSA- and NaCl-induced aggregates were compared, revealing a higher occurrence of side-by-side NR assemblies for the BSA-induced aggregates (Fig. 3, C and D, and Fig. S28-S29). These structural differences were derived from electron imaging

of samples on planar support, thus leaving open the intriguing question of true BSA-templated 3D chiral assembly. A potential scaffolding by BSA to yield chiral assemblies of Au NRs is certainly possible based on the reported use of biomolecules as templates for chiral NP assembly. (*21, 23, 35*) To conclusively answer this question, we performed cryo-electron microscopy (cryo-EM) imaging of NR-BSA aggregates that were frozen from their solution phase conformations. The tilt series images of an Au NR-BSA aggregate clearly indicate twists among neighboring side-by-side NRs (Fig. 3E and Movie S3), strongly supporting chiral templating by BSA.

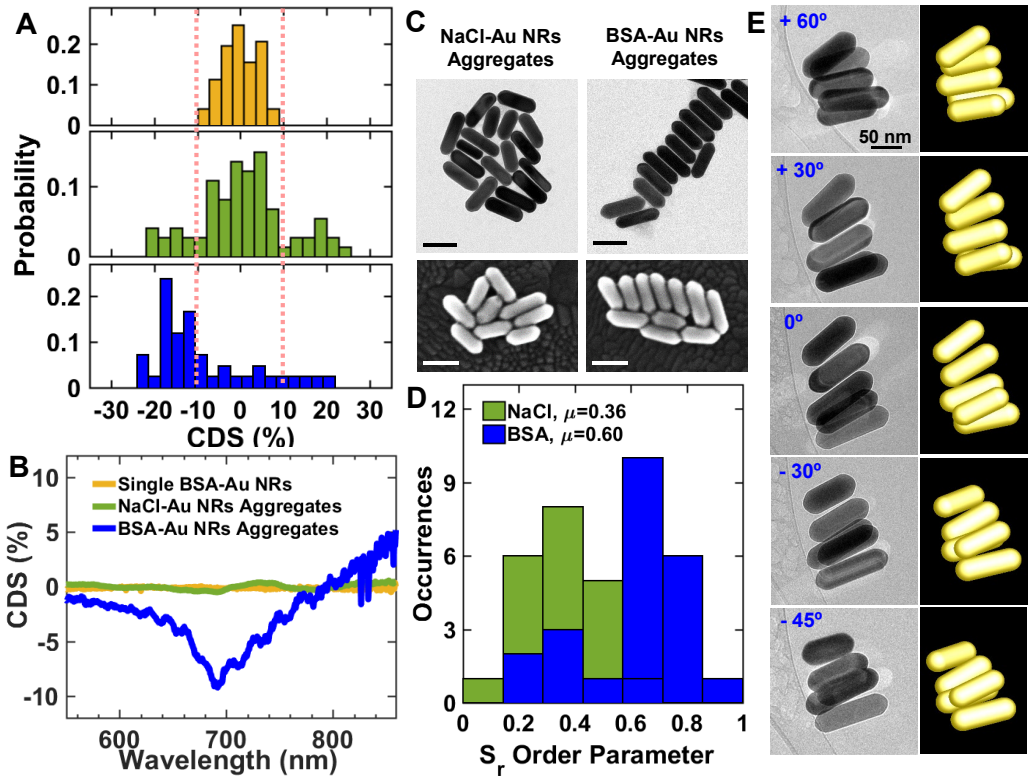

Fig. 3. Role of BSA in PCCD: connecting the single-particle and ensemble levels. (**A,B**) Histogram of CDS maxima (A) and sub-ensemble averaged CDS spectra (B) obtained from single-particle measurements performed on single BSA-Au NRs, NaCl-induced NR aggregates, and BSA-induced aggregates. Only the subensemble CDS spectrum for BSA-induced aggregates shows an overall signal that matches the ensemble spectrum in Fig. 1A, indicating that both the formation of aggregates and the presence of BSA are necessary. (**C**) BSA mediates a predominant side-by-side assembly of gold NRs while more random aggregates were formed by adding NaCl, as seen in TEM and SEM images (scale bars: 100 nm). (**D**) Histogram of the order parameter (S_r) calculated for NR aggregates created using BSA and NaCl. S_r is calculated according to $S_r = \frac{\sum_{i=1}^{N_{nr}} M_i}{2(N_{nr}-1)}$, where N_{nr} is the number of NRs in the aggregate and M_i is the number of side-by-side nearest neighbors for NR i = {1, 2, …, N_{nr}}. **(E)** Tomographic tilt series of a frozen Au NR-BSA aggregate sample in a transmission electron microscope and the corresponding

geometric models. In addition to chirality transfer from BSA molecules in "hotspots", these results further suggest that BSA is responsible in aiding the formation of chiral NR assemblies.

In summary, we used a single-particle approach to unravel the origin of chirality from NP-protein complexes. Based on CDS measurements with correlated tomographic reconstruction and electromagnetic simulations, we demonstrate that only aggregated NR-BSA complexes are CD active. Based on cryo-EM and Raman spectroscopy, we can further conclude that BSA-induced nanoparticle aggregation creates chiral nanostructures in solution, as well as hotspots for strong coupling between chiral proteins and surface plasmons, i.e. PCCD. Both effects may work synergistically by creating superchiral near-fields (*28*). The role of BSA is not simply a chiral chromophore but also appears to affect the assembly of the chiral NR-protein complexes.

References and Notes

1. J. Yeom *et al.*, *Science* **359**, 309-314 (2018).
2. Y. Q. Tang, A. E. Cohen, *Science* **332**, 333-336 (2011).
3. K. Banerjee-Ghosh *et al.*, *Science* **360**, 1331-1334 (2018).
4. J. Kumar *et al.*, *P Natl Acad Sci USA* **115**, 3225-3230 (2018).
5. E. Prodan, C. Radloff, N. J. Halas, P. Nordlander, *Science* **302**, 419-422 (2003).
6. J. K. Gansel *et al.*, *Science* **325**, 1513-1515 (2009).
7. N. J. Halas, S. Lal, W. S. Chang, S. Link, P. Nordlander, *Chem Rev* **111**, 3913-3961 (2011).
8. M. Hentschel, M. Schaferling, X. Y. Duan, H. Giessen, N. Liu, *Sci Adv* **3**, (2017).
9. K. W. Smith, S. Link, W. S. Chang, *J Photoch Photobio C* **32**, 40-57 (2017).
10. J. M. Slocik, A. O. Govorov, R. R. Naik, *Nano Lett* **11**, 701-705 (2011).
11. A. O. Govorov, *J Phys Chem C* **115**, 7914-7923 (2011).
12. H. Zhang, A. O. Govorov, *Phys Rev B* **87**, (2013).
13. I. Lieberman, G. Shemer, T. Fried, E. M. Kosower, G. Markovich, *Angew Chem Int Edit* **47**, 4855-4857 (2008).
14. B. M. Maoz *et al.*, *Nano Lett* **13**, 1203-1209 (2013).
15. L. M. Kneer *et al.*, *ACS Nano* **12**, 9110-9115 (2018).
16. J. George, K. G. Thomas, *J Am Chem Soc* **132**, 2502-2503 (2010).
17. V. A. Gerard, Y. K. Gun'ko, E. Defrancq, A. O. Govorov, *Chem Commun* **47**, 7383-7385 (2011).
18. A. Ben-Moshe, B. Maoz, A. O. Govorov, G. Markovich, *Chem Soc Rev* **42**, 7028-7041 (2013).
19. R. Y. Wang *et al.*, *J Phys Chem C* **118**, 9690-9695 (2014).
20. S. Hou *et al.*, *Phys Chem Chem Phys* **17**, 8187-8193 (2015).
21. H. Shinmori, C. Mochizuki, *Chem Commun* **53**, 6569-6572 (2017).
22. X. B. Shen *et al.*, *Nanoscale* **6**, 2077-2081 (2014).
23. A. Kuzyk *et al.*, *Nature* **483**, 311-314 (2012).
24. W. Ma *et al.*, *Chem Rev* **117**, 8041-8093 (2017).
25. S. Dominguez-Medina *et al.*, *ACS Nano* **10**, 2103-2112 (2016).
26. L. Y. Wang *et al.*, *ACS Photonics* **2**, 1602-1610 (2015).
27. A. Rogozea *et al.*, *J Phys Chem B* **116**, 14245-14253 (2012).
28. E. Hendry *et al.*, *Nat Nanotechnol* **5**, 783-787 (2010).
29. K. W. Smith *et al.*, *ACS Nano* **10**, 6180-6188 (2016).
30. J. M. Abendroth *et al.*, *J Am Chem Soc*, (2019).
31. J. Y. Kim *et al.*, *Sci Adv* **4**, (2018).
32. Y. Fang, N. H. Seong, D. D. Dlott, *Science* **321**, 388-392 (2008).
33. S. M. Nie, S. R. Emery, *Science* **275**, 1102-1106 (1997).
34. K. Kneipp *et al.*, *Phys Rev Lett* **78**, 1667-1670 (1997).
35. X. L. Wu *et al.*, *J Am Chem Soc* **135**, 18629-18636 (2013).
36. J. Olson *et al.*, *Chem Soc Rev* **44**, 40-57 (2015).
37. C. P. Byers *et al.*, *J Phys Chem B* **118**, 14047-14055 (2014).
38. P. B. Johnson, R. W. Christy, *Phys Rev B* **6**, 4370-4379 (1972).
39. K. W. Smith *et al.*, *J Phys Chem C* **122**, 13259-13266 (2018).
40. G. J. Zhai, J. S. Yang, N. Cue, X. S. Wang, *Thin Solid Films* **366**, 121-128 (2000).
41. M. C. Chen, R. C. Lord, *J Am Chem Soc* **98**, 990-992 (1976).
42. M. Kahraman, I. Sur, M. Culha, *Anal Chem* **82**, 7596-7602 (2010).

43. R. Foucault, R. L. Birke, J. R. Lombardi, *Langmuir* **19**, 8818-8827 (2003).

Acknowledgments

The authors thank the Rice University Shared Equipment Authority and Electron Microscopy Center for instrument use and technical assistance.

Funding: This work was funded by the Robert A. Welch Foundation (C-1664 to S.L. and C-1787 to C.F.L.) and the National Science Foundation (CHE1507745 and CHE1903980 to S.L.). Q.Z. acknowledges support from the Smalley-Curl Institute at Rice University through a J. Evans Attwell-Welch Postdoctoral Fellowship. T.M.H., K.W.S., and L.A.M. acknowledge support from the National Science Foundation through a Graduate Research Fellowship (1842494). A.X.D. and J.A.D. acknowledge support from the SLAC National Accelerator Laboratory. D.H.C. acknowledges support from Stanford School of Medicine.

Author contributions: S.L., C.F.L., and Q.Z. conceived and designed the experiments. Q.Z., T.M.H., K.W.S., L.W., R.B., and L.A.M. performed the ensemble and single-particle experiments and data analysis. S.A.H.J. and Q.Z. conducted numerical simulations. Q.Z. and H.G. performed the HAADF-STEM imaging and tomographic reconstruction. A.X.D. and D.H.C performed the cryo-EM sample preparation and imaging. J.A.D. supervised the cryo-EM measurements. Q.Z., C.F.L., and S.L. co-wrote the paper. S.L. and C.F.L supervised the entire study. All authors contributed to the final version of the paper.

Competing interests: None declared.

Data and materials availability: All (other) data needed to evaluate the conclusions in the paper are present in the paper or the Supplementary Materials.

Supplementary Materials:

Materials and Methods

Figures S1-S29

Movies S1-S3

References (*36-43*)